Atomic Level Distributed Strain within Graphene Divacancies from Bond Rotations

Qu Chen[1], Alex W. Robertson[1], Kuang He[1], Chuncheng Gong[1], Euijoon Yoon[2], Gun-Do Lee[2], Jamie H. Warner[1*]*

[1]Department of Materials, University of Oxford, Parks Road, Oxford, OX1 3PH, United Kingdom

[2]Department of Materials Science and Engineering, Seoul National University, Seoul, 151-742, Korea

*Jamie.warner@materials.ox.ac.uk; gdlee@snu.ac.kr

Abstract.

Vacancy defects play an important role in influencing the properties of graphene and understanding their detailed atomic structure is crucial for developing accurate models to predict their impact. Divacancies (DVs) are one of the most common defects in graphene and can take three structural different forms through various sequences of bond rotations to minimize the energy. Using aberration-corrected transmission electron microscopy with monochromation of the electron source, we resolve the position of C atoms in graphene and measure the C-C bond lengths within the three DVs, enabling a map of bond strain to be generated. We show that bond rotations reduce the maximum single bond strain reached within a DV and help distribute the strain over a larger number of bonds to minimize the peak magnitude.

KEYWORDS: Graphene, Defects, Divacancy, TEM, Aberration-correction, DFT

Understanding the structure and behavior of point defects is vital to exploiting the potential of graphene in nano-electronic applications, such as semiconductor devices.[1,2] Point defects in graphene influence the magnetic and electronic properties by disrupting the periodic structure of graphene.[3–6] Removing carbon atoms from the bulk graphene lattice produces vacancies, such as monovacancies (MVs), divacancies (DVs), and multi-vacancies, which can migrate and agglomerate together to form more complex defect structures.[7] The DV consisting of a pentagon-octagon-pentagon (5-8-5) structure forms easily from a monovacancy by removing one of the three under-saturated carbon atoms. Reconstruction is achieved by bonding of all three nearest carbon neighbors, i.e., to maintain a sp^2 hybridization state.[8–10] This reconstruction process and loss of carbon atoms is likely to lead to changes in the electronic charge density within certain bonds in the DV and this will influence the bond lengths within and around the defect. The 5-8-5 DV can transform into the triple pentagon-triple heptagon (555-777) DV by an in-plane 90° rotation of one of the two shared bonds between the pentagons and octagon (highlighted in figure 1e). Similarly, 555-777 DV can further evolve into the quadruple pentagon-hexagon-quadruple heptagon (5555-6-7777) DV by one more Stone-Wales (SW) bond rotation (highlighted in figure 1i).[11–14]

The atomic resolution imaging of isolated point defects in graphene can be achieved using aberration-corrected transmission electron microscopy (AC-TEM).[8,15,16] At the accelerating voltage of 80 kV, a carbon atom can be sputtered out from the bulk graphene lattice by a focused electron beam, which often then leads to the removal of a second carbon atom due to the smaller threshold energy for removing an under-saturated carbon atom.[7] The mechanism for electron induced carbon atom ejection in graphene at an 80 kV accelerating voltage is complex, but is likely due to interactions involving mobile surface adatoms to give rise to what is known as the chemical etching effect. This lowers the energy threshold for sputtering. If the beam current density is kept

low, then this chemical etching process is drastically reduced and graphene can be imaged by AC-TEM at 80kV for extensive periods of time without further atom ejection. This allows the study of defect structures at atomic resolution. However, the low accelerating voltage unavoidably leads to limited resolution, providing a challenge to precisely locating the position of each carbon atom in graphene. Monochromation of the electron source is one way to reduce chromatic aberration effects and increase spatial resolution to ~80pm at 80kV.[17–19].

Previous work has explored the formation and dynamics of divacancies in graphene.[11,20,21] Theoretical calculations indicate that bond rotations lead to lower energy divacancy defects.[20] In this report, we study AC-TEM images of the three types of divacancies with sufficient spatial resolution to resolve individual C-C bond lengths. We use multi-frame averaging to substantially increase the signal to noise ratio and this enables more accurate measurements of atomic positions. By combining our experimental AC-TEM images with multislice image simulations based on density functional theory (DFT) calculations we are able to understand the effect of bond rotations on the local strain in the divacancy structures. The local defect area should ideally be planar, as the out-of-plane ripples of graphene give deviations in apparent bond length measurements for the two-dimensional projections of the three-dimensional object.[22–24] We evaluate the flatness of each divacancy region with the help of the DFT calculated models, where each atom has a specific position in three-dimensional space. To further explore the influence of a divacancy defect on its surrounding hexagonal neighbors, geometric phase analysis is used to map the strain field around the three types of the divacancy defects.

Results and Discussion

A series of atomic models shown in figure 1 demonstrates a schematic illustration of the formation of a divacancy and how it evolves into more complicated divacancy structures by bond rotations.

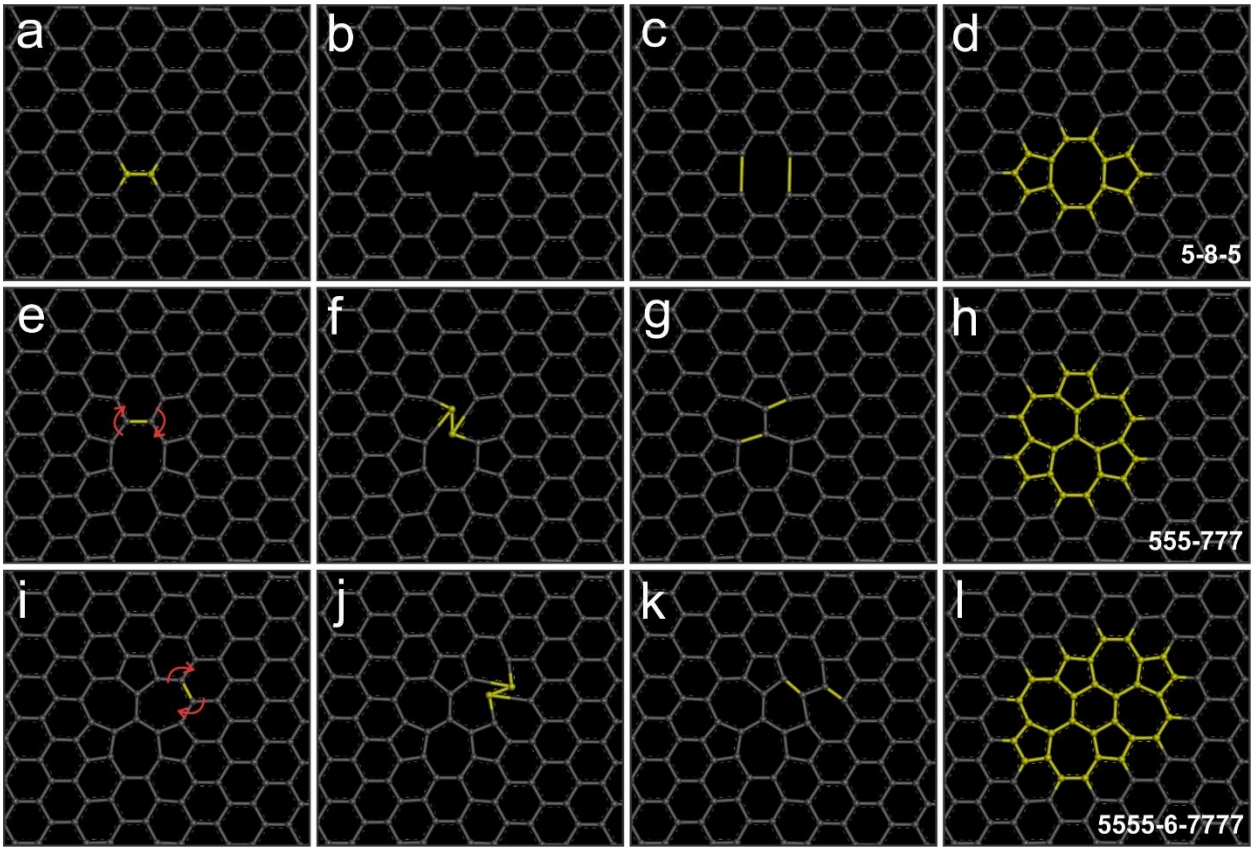

Figure 1 Schematic atomic models showing the 585 divacancy defect and its relation to the 555-777 and 5555-6-7777 divacancy defects by bond rotation.

Figures 2(a)-(c) show an AC-TEM image, bond length measurement and plot of bond strain for an isolated 5-8-5 divacancy defect with the bond length values marked in picometers. Figures 2(d)-(e) show the the multislice image simulation, with corresponding bond lengths and bond strains. The reference C-C bond length shown in the lower right of figure 2(a) is the average bond length of pristine graphene measured far from the defect structure, averaged over many bond measurements. The bond lengths in the AC-TEM image are measured by box-average intensity profiles and subsequently fitted to double Gaussian curves, similar to previous reports.[17,25] The bond length values displayed in figure 2(d) are measured using double Gaussian fitting from the image simulation. The bond lengths based on the atomic coordinates from DFT calculations (figure

S1a) are compared to those calculated from the measurements on simulated images by Gaussian fitting (figure S1c) and show only a small amount of noise error is generated from the measurement process. The coloured bonds shown in the atomic models (figure 2(c) and 2(f)) visually illustrate the bond length variations (BLVs) within the defect area, with the values calculated by dividing every measured or calculated bond length (B_m, or B_c) in the defect by the reference bond distance (B_r), i.e. BLV = B_m/B_r. The warm colours (orange-red) indicate bond elongation (BLV> 1) while the cold colours represent contraction of a bond (BLV<1). The noise level in the TEM image is determined by the standard deviation of the reference unstrained bonds (see figure S4 in supporting information for bond lengths for pristine graphene), thus when the measured bond length is longer than 147 pm or shorter than 139 pm, the bond length variation is beyond two standard deviations and has statistical significance. Correspondingly, the deformation ratio must be higher than 1.03 or lower than 0.97. The most significant elongation occurs at the interface between the octagon and pentagons, which are 17.5% and 15.4% elongated respectively from the experimental result. The theoretical calculated result agrees well with the TEM result, but with a slightly higher elongation value of 19.7%. These regions of bond elongation are indicated with small white dashed ellipses in figures 2(c) and 2(f). The four bonds at the two ends of the octagons are also slightly elongated with an average 7%. Compression is detected at the end of the two pentagons, indicated with the larger white dashed ellipses. However the contraction is not as certain as the elongation measurements due to it being comparable with the noise level.

After bond rotation of the 5-8-5 DV to the 555-777 DV, the bond lengths within the defect area also vary significantly (figure 3). Overall, the range of the bond lengths in the 555-777 DV is narrower than the original 5-8-5 DV defect. The most elongated bonds are the six bonds shared by the three heptagons and the three pentagons, with average elongation ratio of 1.10 and 1.07 for

TEM and DFT result respectively. This fits in well with the report by Rasool *et al*, who explored pentagon-heptagon structures along graphene grain boundary and found most of the shared bonds between pentagon and heptagon have been elongated to some extent.[25] The surrounding bonds around the 555-777 defect shows regular change: the bonds at the ends of the 7-membered rings are elongated while the bonds at the ends of the 5-membered rings are contracted, indicated with white dashed ellipses.

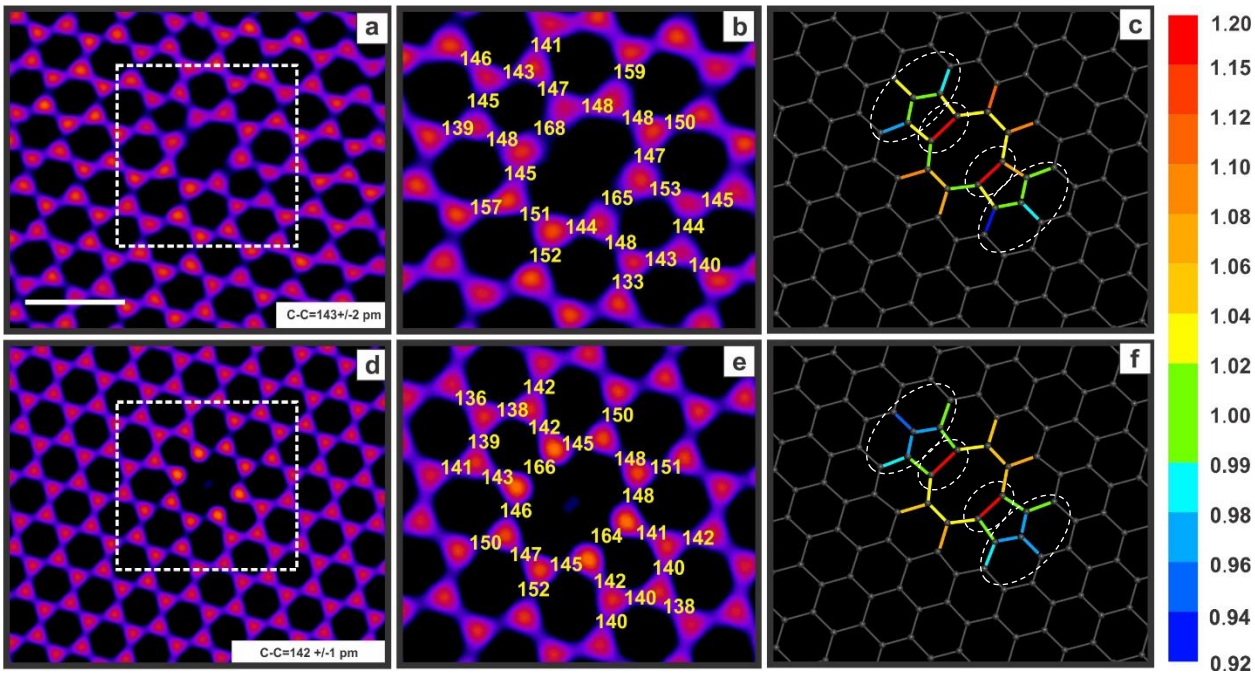

Figure 2 Bond length variations in 585 defect. a) TEM image of an isolated 585 divacancy with a 'fire' colour LUT for display. Scale bar: 500 pm. b) TEM image showing the region in the white dashed box of a) at the defect with bond length values in picometers. c) Atomic model showing the ratio of local bond length to the average bond length of pristine graphene based on TEM. d) Multislice image simulation based on the DFT calculation of a 585 defect. e) Simulation image showing the region in the white dashed box of d) at the defect with bond length values directly determined from the image simulation. f) Atomic model showing the ratio of local bond length to the average bond length of pristine graphene based on DFT. Small

white dashed ellipses indicate regions of bond elongation, whilst larger white dashed ellipses indicate regions of bond contraction.

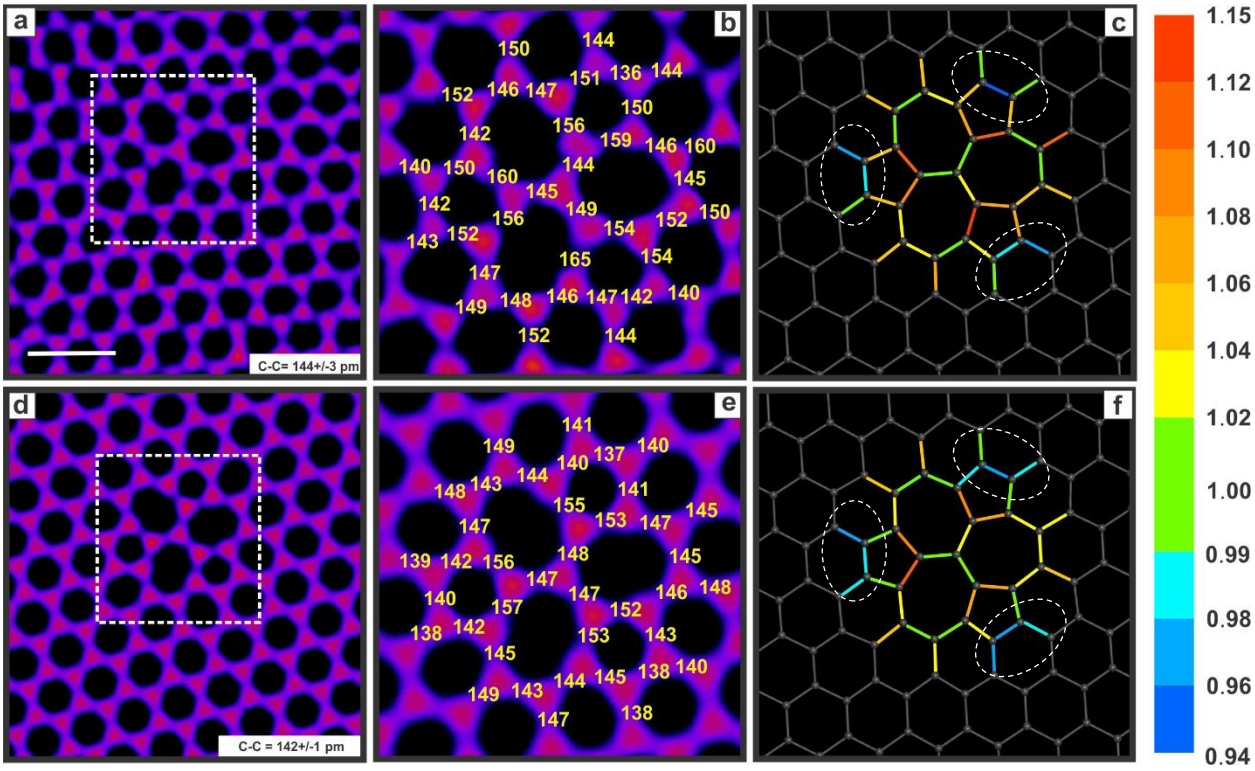

Figure 3 Bond length variations in 555-777 defect. a) TEM image of an isolated 555-777 divacancy with a 'fire' colour LUT for display. Scale bar: 500 pm. b) TEM image showing the region in the white dashed box of a) at the defect with bond length values in picometers. c) Atomic model showing the ratio of local bond length to the average bond length of pristine graphene based on TEM. d) Multislice image simulation based on the DFT calculation of a 555-777 defect. e) Simulation image showing the region in the white dashed box of d) at the defect with bond length values directly determined from the image simulation. f) Atomic model showing the ratio of local bond length to the average bond length of pristine graphene based on DFT.

A second bond rotation converts the 555-777 DV into the larger 5555-6-7777 DV, shown in figure 4. Unlike the former two DV defects examined in figures 2 and 3, where elongated bonds were observed, the bond length variation within the 5555-6-7777 DV defect structure is reduced.

However, the spatial trend of the elongation and contraction for 585 and 555-777 structures is still apparent in the 5555-6-7777 defect. The joint bonds between pentagons and heptagons are all elongated, although the deformation ratio decreases to 1.03-1.05. Shortened bonds are observed at the ends of the pentagons (the left and right ends), just like the situation of the former two DV structures.

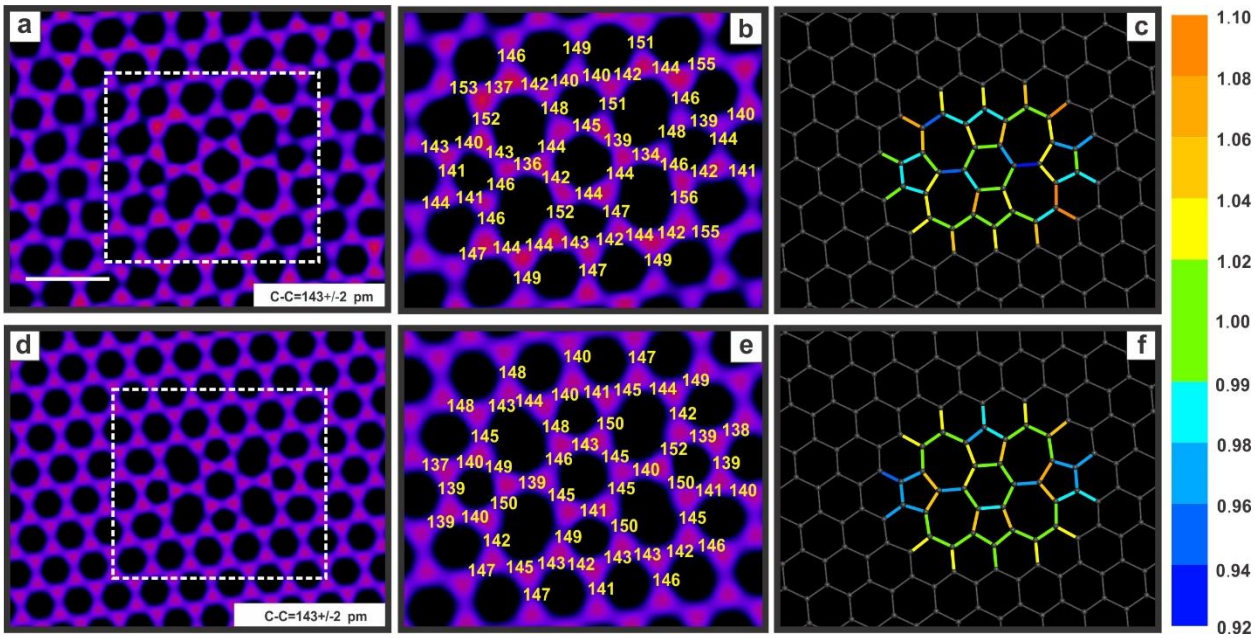

Figure 4 Bond length variations in 5555-6-7777 defect. a) TEM image of an isolated 5555-6-7777 divacancy with a 'fire' colour LUT for display. Scale bar: 500 pm. b) TEM image showing the region in the white dashed box of a) at the defect with bond length values in picometer. c) Atomic model showing the ratio of local bond length to the average bond length of pristine graphene based on TEM. d) Multislice image simulation based on the DFT calculation of a 5555-6-7777 defect. e) Simulation image showing the region in the white dashed box of d) at the defect with bond length directly determined from the image simulation. f) Atomic model showing the ratio of local bond length to the average bond length of pristine graphene based on DFT.

The DFT calculated charge density maps for the three types of divacancies are shown in figure 5. The most conclusive charge density attenuation among the three mappings is at the interface between the pentagons and octagon in 585 divacancy, indicated with a black arrow in figure 5d. This matches the experimental results showing the two bonds are the most elongated, figure 2. Typically, the shared bonds at the pentagon-heptagon interfaces have lower charge density, figure 5e and 5f. Some of this is detected in figures 3 and 4 as bond elongation with varying degree.

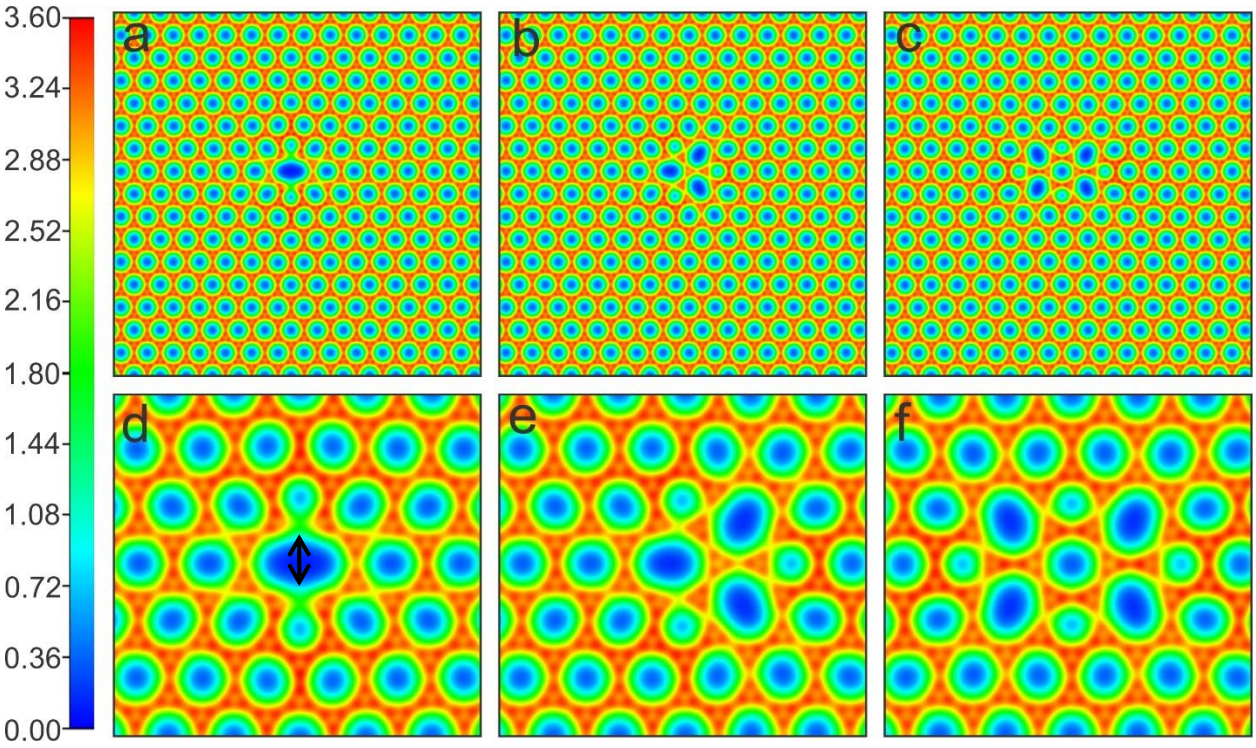

Figure 5 Total charge density of the a, d) 585 divacancy, b, e) 555-777 divacancy and c, f) 5555-6-7777 divacancy calculated by DFT for the atomic models shown in figure S1 to S3. The unit of charge density is e/a_0^3 (electron/Bohr radius^3). Black arrow indicates bonds with largest charge depletion at the pentagon-octagon interface.

To further explore the distribution of the bond lengths within the three types of divacancy defects, histograms (figure 6) with Gaussian fits are plotted for both TEM and DFT results from figure 2 to figure 4. The distribution plot with the bond length values based on the DFT calculated models is shown in figure S5 in supporting information. It can be seen that experimental and theoretical results share the same trend. With the addition of bond rotations, both distribution width and average bond length are reduced, indicating that the bond rotation decreases the peak value for elongated and compressed bonds (the average bond length and standard deviation are listed in supporting information table S1). The larger local defect area also contributes to the reduced average bond length as more bonds are involved in to share the variation caused by the two missing carbon atoms. Therefore, 555-777 and 5555-6-7777 are more stable than the original DV defect (585), which is also confirmed by the energy state of the three defects: the formation energy of 585 is 0.53 eV higher than 555-777, which is the lowest energetic structure among the three divacancies, while the difference in the formation energy between the 5555-6-7777 and the 555-777 is small (~0.1eV) according to our DFT calculation. Similar results of the relative formation energies of the three DVs have also been reported by Leyssale and Vignoles.[13]

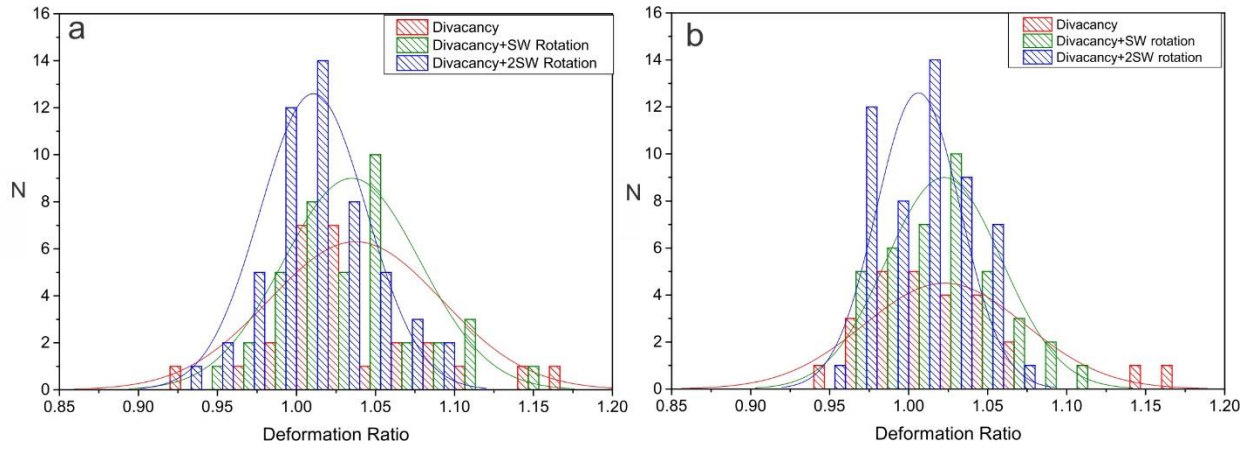

Figure 6 Histograms of the bond length ratios of the three divacancies measured from both TEM (a) and DFT (b) results, with Gaussian distribution fitting.

Defective graphene does not have perfect flat (2D) structure due to out-out-plane distortions that help stabilize the strain in the bonds. Atomic models calculated by DFT show the height variations within a graphene sheet and can be used to determine the effect of out-of-plane distortions on the apparent bond length contraction in the 2D projection of a TEM image. Figure 7 (a-c) shows the z-plot (out-of-plane distance) of graphene with divacancies at the central area. The colour map shows directly the height change, with red regions referring to the peaks while blue regions indicating the valleys. The colour scale bar is in Angstroms. The defect is in the pale blue and green area, with much less distortion than the edge area, where dark blue and red are dominating. The tilt angle along x or y direction is defined as the height variation within a single pixel (pixel $= 0.1 \times 0.1$ Å^2).

$$\frac{|z_1 - z_2|}{0.1} = \tan\theta$$

Where z is the height in Å, 0.1 Å is the pixel width, and θ the tilt angle of the bond. The tilt-angle maps for the three DVs along the x and y directions are shown in figure 7d to 7i. The biggest tangent value within the maps for the 585 DV is around 0.11, indicated by the white arrow in figure 7d, thus theta is 6.3°. The height changes more gradually around the defect area (the centre of the defect is marked by the white cross, and the dashed circle highlights the fourth nearest hexagons around the defect), with θ smaller than 4°. Figure 7j to 7o demonstrate the deviation of projected distance from true distance caused by the tilting angle in x and y directions. The deviation is determined by

$$1 - \cos\theta = 1 - \cos(\tan^{-1}\frac{|z_1 - z_2|}{0.1})$$

Among the six maps, the largest deviation value is 6.0×10^{-3} (0.6%) (shown by the white arrow in figure 7j), which is significantly smaller than the observational error during the bond length measurement. The deviation is even smaller within the defect regions, from 0 to 0.24%. Therefore, it can be concluded from these maps that the graphene lattice possesses sufficient flatness around the DV defect regions and out-of-plane distortions are negligible for impacting bond length measurements.

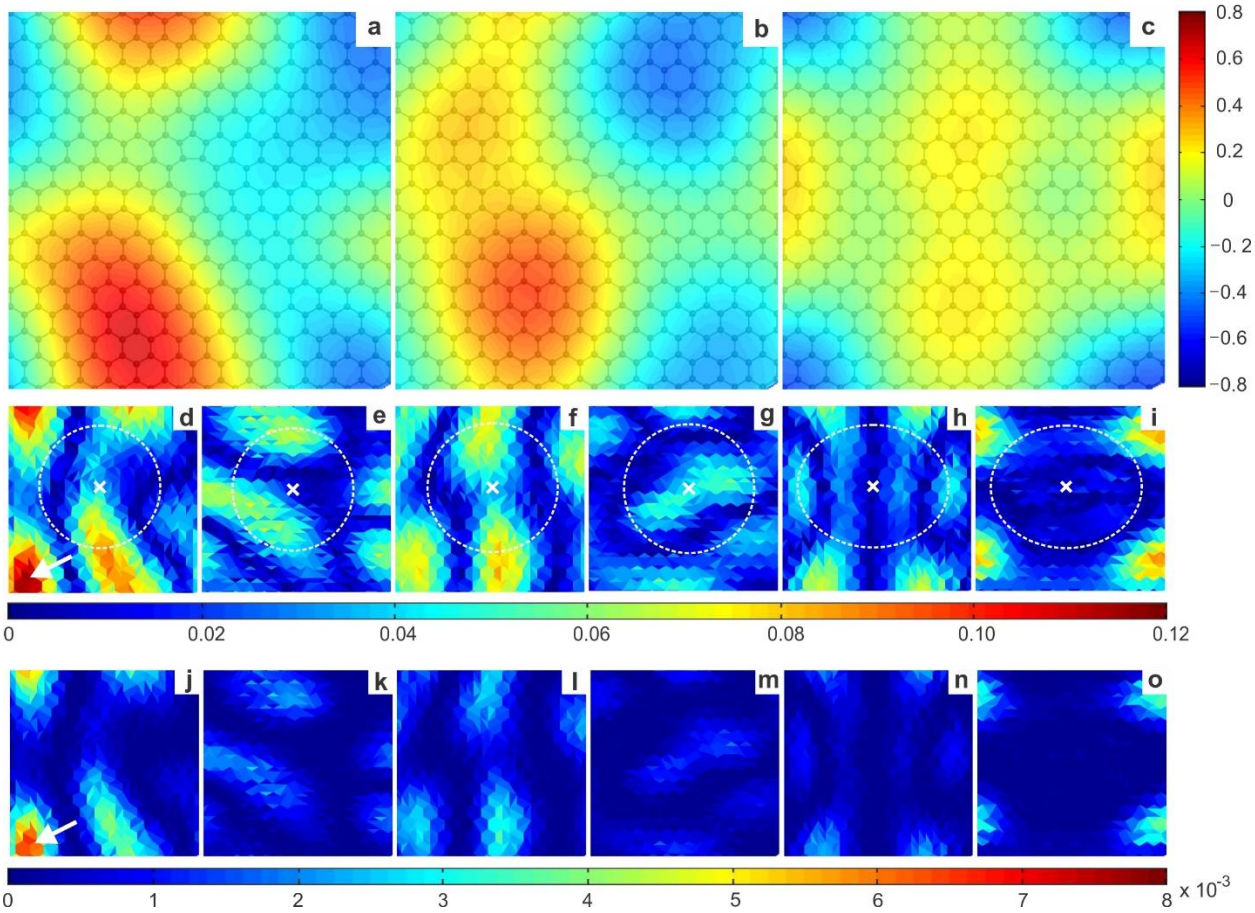

Figure 7 (a-c) Z height mappings for 585 (a), 555-777 (b) and 5555-6-7777 (c) based on the DFT calculation. d-i) Tilt angle maps for 585 (d, e), 555-777 (f, g), and 5555-6-7777 (h, i). d, f, h) Along x direction: $\partial z/\partial x$. (e, g, i)Along y direction: $\partial z/\partial y$. (j-o) Deviation of projected distance from the true value by height fluctuation for 585 (j, k), 555-777 (l, m), and 5555-6-7777 (n, o). (j, l, n) Along x direction.

(k, m, o) along y direction. The white dashed ellipses in d-i correspond to the fourth nearest hexagons to the defects, with white crosses at the defect centres.

Introduction of a DV defect disrupts the periodic structure of the graphene lattice and is likely to give rise to large strain fields that could extend out to the surrounding hexagonal lattice. Geometric phase analysis (GPA) is a useful tool to show the four types of strain (normal strain and ε_{yy}, shear strain ε_{xy}, and rotation) by plotting strain in colour scale.[26] As GPA investigates the periodicity deviation in 2D projection, it cannot distinguish the strain caused by bond elongation (contraction) or out-of-plane distortion. However, we have already confirmed that the largest tilting angle among the three defects and their surrounding graphene lattice (from the defect edge to the fourth nearest hexagon) is 4°, beyond the sensitivity of GPA. In recent work we showed that the 'apparent' strain measured as a d-spacing lattice change (not real strain), caused by out-of-plane distortions, give apparent bond shorting when imaged by AC-TEM requires the tilting angle to reach at least 15°.[22] This means that in our case, the strain values can be regarded as pure in-plane distortions generated from altered bond lengths and orientation.

Figure 8 shows the strain maps from TEM images of the three DV defects (strain maps for DFT image simulations are in figure S6). The strain maps for DFT simulation images match the experimental results well. The four concentric ellipses (black, red, blue and violet) represent the range from the first nearest neighbors (black) to the fourth (violet). The colour look-up table (CLUT) palette covers the range from -50% to 50% for the normal and shear strain field and ± 0.5 radians for the rotation, with blue corresponding to 0. It can be seen that a strain field is measured outside the defects, oval profile plots are conducted for surrounding hexagonal rings to give a measurement of strain as a function of angle around the oval.

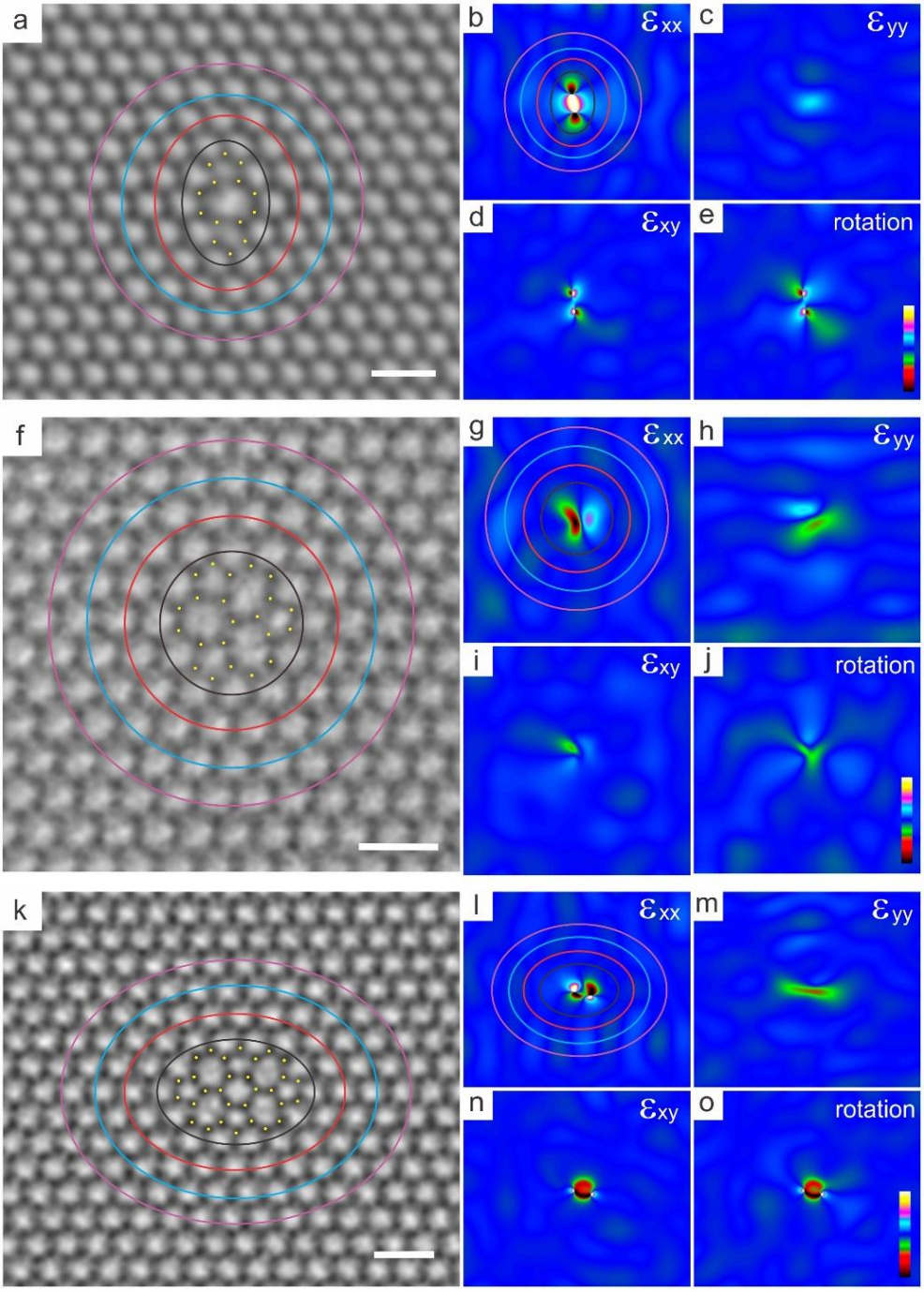

Figure 8 Strain mappings of the three DVs based on TEM images. Scale bar: 500 pm. (a, f, k) Gray scale TEM image of 585, 555-777 and 5555-6-7777 defect (b-e, g-j, l-o) Strain mappings for the three DVs with the type of strain marked at upper-right corner in each mapping. The CLUT palette covers the range from -50% to 50% for the normal and shear strain field and ± 0.5 radians for the rotation. The four

ellipses in both TEM images and ε_{xx} mappings correspond to the most (black), second (red), third (blue) and fourth (violet) nearest hexagonal rings from the defect boundaries.

Figure 9 shows the normal strain in x direction (ε_{xx}) and rotation along the first nearest hexagonal neighbors of the three defects (black ellipses shown in each TEM image, DFT simulation). The oval profiles for ε_{yy} and ε_{xy} are shown in figure S7 in supporting information. The experimental and theoretical results show good matches. The profiles can be regarded as fluctuating around 0 with various amplitudes, due to the symmetrical structure of the defects. The background noise is detected by plotting four oval profiles far away from the defects (one for each strain type). The background noise level is approximately -0.02 to 0.02 for whichever type of strain (See supporting information figure S7e). For both ε_{xx} and rotation, the 585 DV defect has the largest distortion on surrounding lattice, from -0.08 to 0.08 in x direction. The largest positive normal strain happens at the left and right sides of the octagon, which also corresponds to the bond length measurement results, where the four bonds adjacent to the octagon are all elongated. Because of the absence of two carbon atoms, the surrounding hexagonal rings also rotate to accommodate the reconstruction, which is why there is obvious rotation emerging at the four hexagons adjacent to both the pentagons and octagon. The strain in the nearest neighbors decays with the addition of a bond rotation. For the 555-777 DV defect, the amplitude is about 0.04. It can be seen that after two bond rotations the strain variation is comparable to the background noise, which means for the 5555-6-7777 DV defect, the strain is mainly limited to within the defect itself.

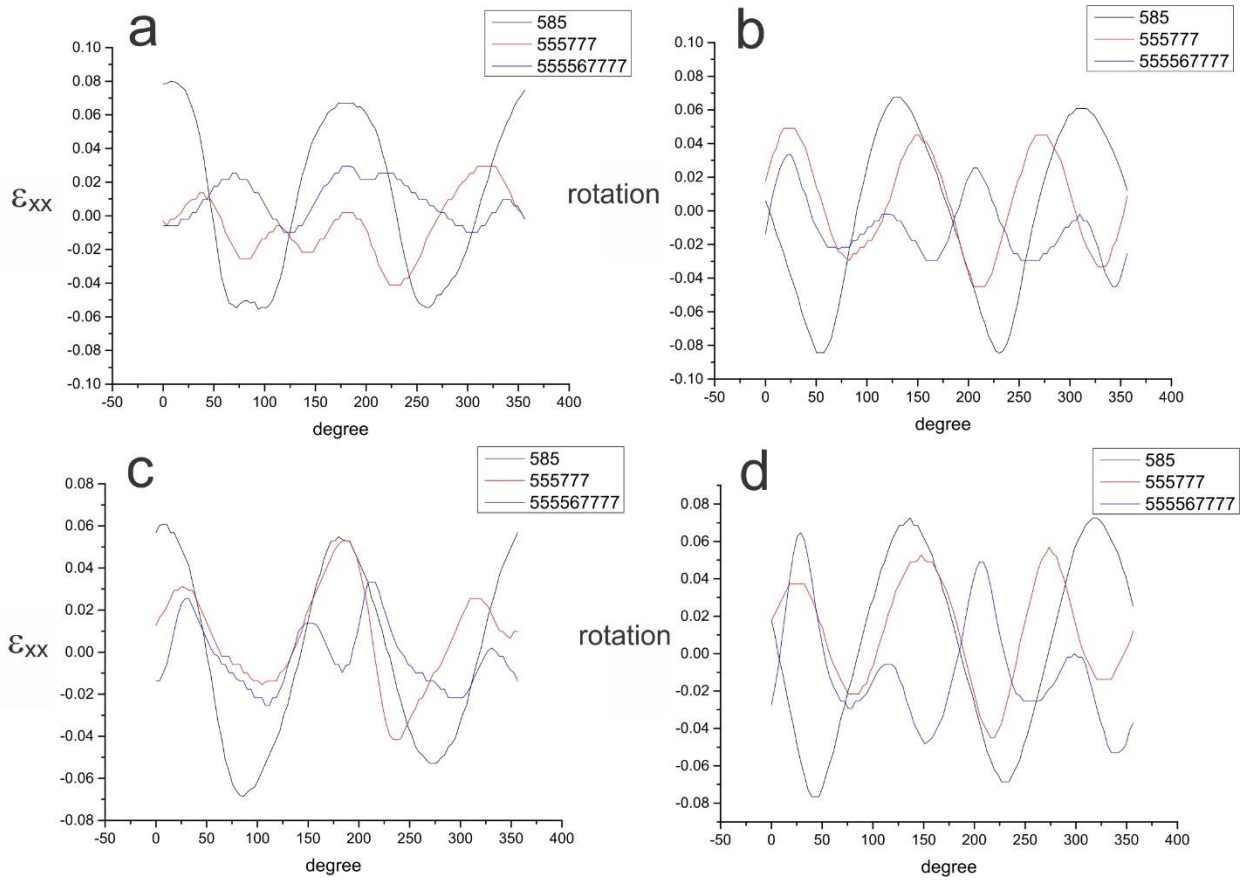

Figure 9 Oval strain profiles of a) ε_{xx} (TEM), b) rotation (TEM), c) ε_{xx} (DFT), d) rotation (DFT) along the nearest hexagonal neighbors.

To examine how strain levels vary with distance from the boundaries of the defects, more oval profiles from the first to fourth nearest neighbors are plotted (the ellipses are shown in figure 8, and the largest ellipse corresponds to the white dashed ellipses in height tilt-angle maps). As stated earlier, the oval strain profiles can be treated as oscillations around 0, therefore, standard deviation (SD) is a plausible way to simplify a profile and to represent the strain state. Higher SD value indicates higher strain variation along the oval. Figure 10 shows the standard deviation values for ε_{xx} and rotation from the first to fourth nearest neighbors, with the upper two profiles for TEM results and the lower two for DFT simulations (the plots for ε_{yy} and ε_{xy} are in figure S8 in supporting information). It is worth pointing out that the SD for the background is about 0.01,

which are the pale blue regions highlighted in the figure. It is obvious that strain decays with the increase of the distance to the defect, and the strain along the third nearest hexagon is submerged into the background noise level (two standard deviations), no matter which type of divacancy and strain. 585 defect can expand its strain to the second nearest hexagons, as shown in the ε_{xx} and rotation profiles. After one SW rotation, the strain field narrows down to the nearest neighbors. However, when one more SW rotation occurs, the strain is further compensated by the defect itself, as almost all standard deviation of the 5555-6-7777 defect is at the same level as the background.

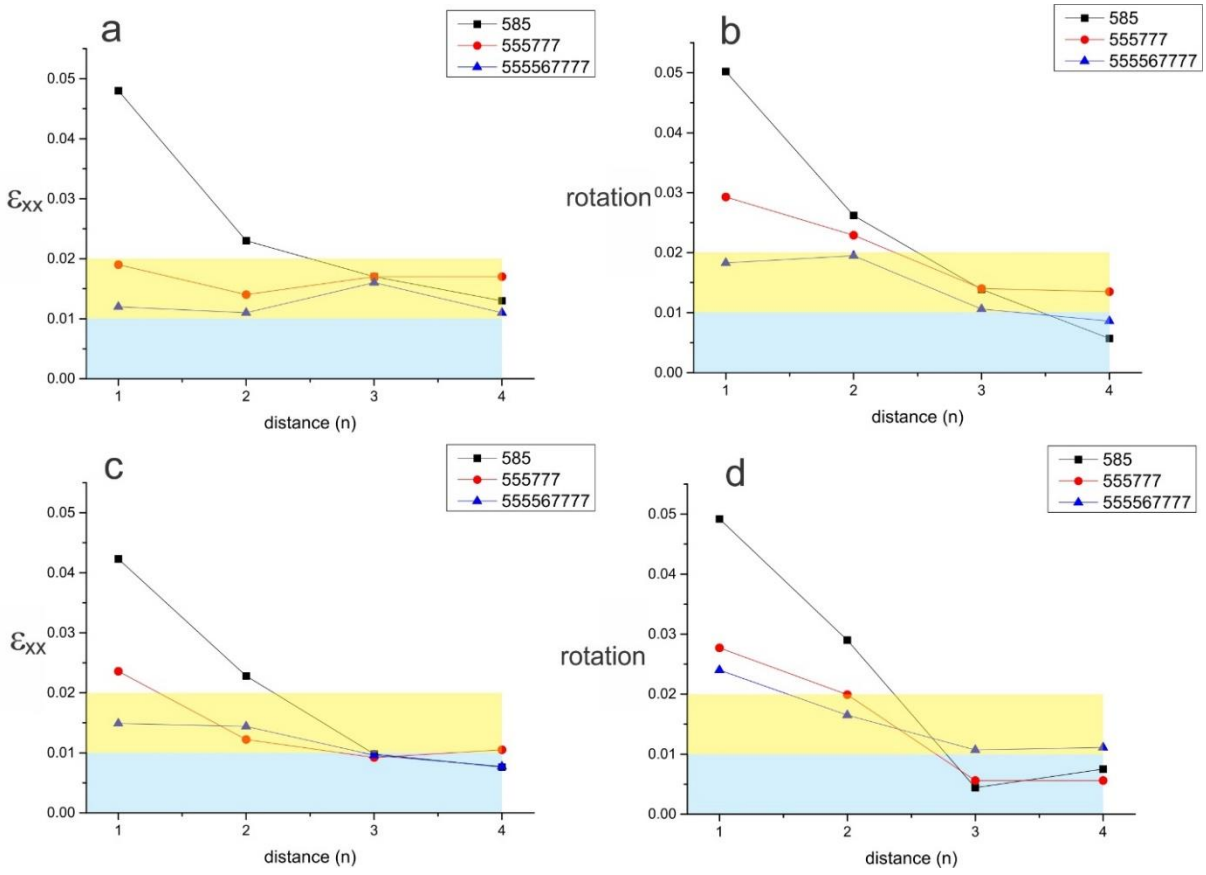

Figure 10 Standard deviations of ε_{xx} and rotation from the first to fourth nearest neighbors, (a, b) From TEM strain mappings. (c, d) From DFT strain mappings. The pale blue regions (0-0.01) represent for the standard deviation of the background and the pale yellow boxes reach the value of two standard deviations (0.02).

Conclusion

We have explored the bond length variations within the three types of divacancy defects. The significant bond length changes caused by the removal of two carbon atoms from a small local region are reduced by the involvement of bond rotations, which has been confirmed by the DFT calculated results. The local areas of the divacancy defects possess reasonable flatness, where the out-of-plane distortion caused by the rippling nature of graphene can be neglected in measured bond lengths. We have studied strain distributions within the hexagonal neighbors around the three divacancies, and the original divacancy (585) has the largest influence to the surrounding 6-numbered rings. The strain is released by SW rotation and for 5555-6-7777 defect, the strain is limited to the defect, with no obvious strain beyond the defect boundary. These experimental and theoretical results are the visualized evidence for the fact that 555-777 and 5555-6-7777 divacancy structures are more energetic favorable than the original 585 divacancy due to more evenly distributed bond lengths and released strain field. The large bond strain found in interface between pentagon and octagon rings is likely an explanation for why these are less frequent in larger defect clusters, which are primarily made up of pentagons and heptagons, or 558558 alternating sequences.

Methods

Synthesis and transfer of Graphene. Graphene was synthesized by chemical vapour deposition method using a melted copper catalyst, as previously reported.[27] Copper foil (99.999% purity, 0.1 mm thick, Alfa Aesar) was placed on a molybdenum support (0.1 mm thick), positioned in a furnace, and annealed at 1090 °C under a mixture gas flow of 200 sccm Argon and 100 sccm 25%

hydrogen/75 % argon for 30-60 minutes. The H_2/Ar mixture was then reduced to 80 sccm, with an addition of 1% methane/99% Ar mixture to the system for 90min. The sample was rapidly cooled down to room temperature under a H_2 and Ar atmosphere. The graphene/Cu/Mo stack was then spin coated with PMMA to form a thin film, before the Cu is etched by a $FeCl_3$ solution. The sample is then rinsed several times by HCl and DI water to remove any residual etchant solution. The film was then transferred to a silicon nitride TEM grid containing 2 μm holes, followed by removing PMMA by baking in air at 350 °C overnight. Before imaging, residual contamination on the surface of the TEM sample was eliminated by heating in vacuum at 150 °C.

Simulation Methods

In order to describe the out-of-plane distortion correctly, first, we performed simulated annealing from 3,000 K using a tight-binding molecular dynamics (TBMD) simulation method. With the annealed structures, relaxation using the density functional theory (DFT) calculations was performed to get the optimized structures. In the TBMD simulation, we used the modified environment-dependent tight binding carbon potential.[28] The DFT calculations are performed within the generalized gradient approximation of Perdew−Burke−Ernzerhof (PBE) functional using Vienna ab initio simulation package (VASP) code.[29,30] Vanderbilt pseudopotentials are also used in the DFT calculation.[31] The basis set contains plane waves up to an energy cutoff of 400 eV. The unit cell is constructed by removing two carbon atoms from pristine graphene of 448 carbon atoms. The unit cell is periodically repeated in the lateral direction and contains the vacuum region of 30 Å. We choose only one k point, the Γ point because the unit cell is enough large. When structural relaxations are performed, the structure is fully relaxed until the force on each atom is smaller than 0.02 eV/Å.

Transmission Electron Microscopy. AC-TEM was conducted using Oxford's JEOL JEM-2200MCO field-emission gun transmission electron microscope (operated at accelerating voltage of 80 kV), with CEOS probe and image aberration correctors and a double Wien Filter monochromator (5 μm slit) to reduce the energy spread of electron beam.

Image Process and Analysis. TEM images were processed by Image J, where a bandpass filter (between 100 and 1 pixels) and Gaussian blur were carefully applied to minimize long range uneven illumination without affection to the interpretation of the original information. Multiple frames (5-10) with the exact same structure were averaged to enhance the signal-to-noise ratio. A LUT of 'fire' was used to improve visual inspection of TEM images. Bond lengths were measured by box-average intensity profiles, fitted by double Gaussian curves, to locate the center of the contrast spots in TEM images. Multislice image simulations were performed using JEMS software with supercells, which were constructed using Accelrys Discovery Studio Visualizer.

Supporting Information Available: Bond length measurements from DFT models. Bond length measurements from pristine regions of graphene. Strain mapping data for other strain components. Supporting Information is available free of charge *via* the Internet at http://pubs.acs.org.

Acknowledgements

JHW thanks the Royal Society for support. GDL acknowledges support from the Supercomputing Center/Korea Institute of Science and Technology Information with supercomputing resources (KSC-2014-C3-009) and from the National Research Foundation of Korea (NRF) grant funded by the Korea government (RIAM No. 2010-0012670).

References

(1) Novoselov, K. S.; Falko, V. I.; Colombo, L.; Gellert, P. R.; Schwab, M. G.; Kim, K. A Roadmap for Graphene. *Nature* **2012**, *490*, 192–200.

(2) Arsat, R.; Breedon, M.; Shafiei, M.; Spizziri, P. G.; Gilje, S.; Kaner, R. B.; Kalantar-zadeh, K.; Wlodarski, W. Graphene-like Nano-Sheets for Surface Acoustic Wave Gas Sensor Applications. *Chem. Phys. Lett.* **2009**, *467*, 344–347.

(3) Shi, H.; Barnard, A. S.; Snook, I. K. Site-Dependent Stability and Electronic Structure of Single Vacancy Point Defects in Hexagonal Graphene Nano-Flakes. *Phys. Chem. Chem. Phys.* **2013**, *15*, 4897–4905.

(4) Nair, R. R.; Sepioni, M.; Tsai, I.-L.; Lehtinen, O.; Keinonen, J.; Krasheninnikov, A. V; Thomson, T.; Geim, A. K.; Grigorieva, I. V. Spin-Half Paramagnetism in Graphene Induced by Point Defects. *Nat Phys* **2012**, *8*, 199–202.

(5) Wang, B.; Pantelides, S. T. Magnetic Moment of a Single Vacancy in Graphene and Semiconducting Nanoribbons. *Phys. Rev. B* **2012**, *86*, 165438.

(6) Carr, L. D.; Lusk, M. T. Defect Engineering: Graphene Gets Designer Defects. *Nat Nano* **2010**, *5*, 316–317.

(7) Robertson, A.; Warner, J. Atomic Resolution Imaging of Graphene by Transmission Electron Microscopy. *Nanoscale* **2013**, *5*, 4079–4093.

(8) Robertson, A. W.; Allen, C. S.; Wu, Y. A.; He, K.; Olivier, J.; Neethling, J.; Kirkland, A. I.; Warner, J. H. Spatial Control of Defect Creation in Graphene at the Nanoscale. *Nat Commun* **2012**, *3*, 1144.

(9) Banhart, F.; Kotakoski, J.; Krasheninnikov, A. V. Structural Defects in Graphene. *ACS Nano* **2011**, *5*, 26–41.

(10) Kotakoski, J.; Krasheninnikov, A. V; Kaiser, U.; Meyer, J. C. From Point Defects in Graphene to Two-Dimensional Amorphous Carbon. *Phys. Rev. Lett.* **2011**, *106*, 105505.

(11) Kotakoski, J.; Mangler, C.; Meyer, J. C. Imaging Atomic-Level Random Walk of a Point Defect in Graphene. *Nat. Commun.* **2014**, *5*, 3991.

(12) Kotakoski, J.; Meyer, J. C.; Kurasch, S.; Santos-Cottin, D.; Kaiser, U.; Krasheninnikov, A. V. Stone-Wales-Type Transformations in Carbon Nanostructures Driven by Electron Irradiation. *Phys. Rev. B* **2011**, *83*, 245420.

(13) Leyssale, J.-M.; Vignoles, G. L. A Large-Scale Molecular Dynamics Study of the Divacancy Defect in Graphene. *J. Phys. Chem. C* **2014**, *118*, 8200–8216.

(14) Lee, G.-D.; Wang, C. Z.; Yoon, E.; Hwang, N.-M.; Kim, D.-Y.; Ho, K. M. Diffusion, Coalescence, and Reconstruction of Vacancy Defects in Graphene Layers. *Phys. Rev. Lett.* **2005**, *95*, 205501.

(15) Meyer, J. C.; Kisielowski, C.; Erni, R.; Rossell, M. D.; Crommie, M. F.; Zettl, a. Direct Imaging of Lattice Atoms and Topological Defects in Graphene Membranes. *Nano Lett.* **2008**, *8*, 3582–3586.

(16) Hashimoto, A.; Suenaga, K.; Gloter, A.; Urita, K.; Iijima, S. Direct Evidence for Atomic Defects in Graphene Layers. *Nature* **2004**, *430*, 870–873.

(17) Warner, J. H.; Lee, G. Do; He, K.; Robertson, A. W.; Yoon, E.; Kirkland, A. I. Bond Length and Charge Density Variations within Extended Arm Chair Defects in Graphene. *ACS Nano* **2013**, *7*, 9860–9866.

(18) Mukai, M.; Kaneyama, T.; Tomita, T.; Tsuno, K.; Terauchi, M.; Tsuda, K.; Naruse, M.; Honda, T.; Tanaka, M. Performance of a New Monochromator for a 200 kV Analytical Electron Microscope. *Microsc. Microanal.* **2005**, *11*, 2134–2135.

(19) Warner, J. H.; Margine, E. R.; Mukai, M.; Robertson, A. W.; Giustino, F.; Kirkland, A. I. Dislocation-Driven Deformations in Graphene. *Science* **2012**, *337*, 209–212.

(20) Kim, Y.; Ihm, J.; Yoon, E.; Lee, G. Do. Dynamics and Stability of Divacancy Defects in Graphene. *Phys. Rev. B - Condens. Matter Mater. Phys.* **2011**, *84*, 1–5.

(21) Botello-Mendez, A. R.; Declerck, X.; Terrones, M.; Terrones, H.; Charlier, J.-C. One-Dimensional Extended Lines of Divacancy Defects in Graphene. *Nanoscale* **2011**, *3*, 2868–2872.

(22) Warner, J. H.; Fan, Y.; Robertson, A. W.; He, K.; Yoon, E.; Lee, G. Do. Rippling Graphene at the Nanoscale through Dislocation Addition. *Nano Lett.* **2013**, *13*, 4937–4944.

(23) Fasolino, A.; Los, J. H.; Katsnelson, M. I. Intrinsic Ripples in Graphene. *Nat Mater* **2007**, *6*, 858–861.

(24) Meyer, J. C.; Geim, A. K.; Katsnelson, M. I.; Novoselov, K. S.; Booth, T. J.; Roth, S. The Structure of Suspended Graphene Sheets. *Nature* **2007**, *446*, 60–63.

(25) Rasool, H. I.; Ophus, C.; Klug, W. S.; Zettl, a.; Gimzewski, J. K. Measurement of the Intrinsic Strength of Crystalline and Polycrystalline Graphene. *Nat. Commun.* **2013**, *4*, 2811.

(26) Hytch, M. J.; Putaux, J.-L.; Penisson, J.-M. Measurement of the Displacement Field of Dislocations to 0.03 Å by Electron Microscopy. *Nature* **2003**, *423*, 270–273.

(27) Wu, Y. A.; Fan, Y.; Speller, S.; Creeth, G. L.; Sadowski, J. T.; He, K.; Robertson, A. W.; Allen, C. S.; Warner, J. H. Large Single Crystals of Graphene on Melted Copper Using Chemical Vapor Deposition. *ACS Nano* **2012**, *6*, 5010–5017.

(28) Lee, G.-D.; Wang, C. Z.; Yoon, E.; Hwang, N.-M.; Ho, K. M. Vacancy Defects and the Formation of Local Haeckelite Structures in Graphene from Tight-Binding Molecular Dynamics. *Phys. Rev. B* **2006**, *74*, 245411.

(29) Perdew, J. P.; Burke, K.; Ernzerhof, M. Generalized Gradient Approximation Made Simple. *Phys. Rev. Lett.* **1996**, *77*, 3865–3868.

(30) Kresse, G.; Furthmüller, J. Efficient Iterative Schemes for Ab Initio Total-Energy Calculations Using a Plane-Wave Basis Set. *Phys. Rev. B* **1996**, *54*, 11169–11186.

(31) Vanderbilt, D. Soft Self-Consistent Pseudopotentials in a Generalized Eigenvalue Formalism. *Phys. Rev. B* **1990**, *41*, 7892–7895.

Table of Contents Graphic